Optimized 2-D NUFFTs for Spiral Scanning in MRI

Amedeo Capozzoli, Claudio Curcio, and Angelo Liseno

Abstract – Nonuniform fast Fourier transforms (NUFFTs) must be used for spiral sampling magnetic resonance imaging (MRI) trajectories, because they restore $\mathcal{O}(N \log N)$-complexity processing. Recently we proposed a 1-D NUFFT using an optimized interpolation window, reaching an accuracy close to double precision and gaining almost one order of magnitude in terms of root-mean-square accuracy against state-of-the-art techniques. We here extend it to 2-D and apply the NUFFT to spiral MRI scans. The results show the extreme accuracy of the proposed approach.

1. Introduction

In magnetic resonance imaging (MRI), a Cartesian sampling scheme enables reconstructions with a simple fast Fourier transform (FFT) [1], which is appealing due to its $\mathcal{O}(N \log N)$ computational complexity. However, nowadays data are often collected in non-Cartesian acquisitions, as many radial MRI systems are commercially available. Moreover, the spiral sampling trajectory [2], still at an experimental stage, is gaining much interest due to its speed and simpler generation of field gradients.

The use of a standard FFT to process spiral trajectories breaks down. Spiral processing is more involved due to the sample nonuniformity, requiring more sophisticated algorithms to balance accuracy and computational burden [3–5]. Nevertheless, high accuracy in MRI is of interest [3, 6] in quantitative MRI [7]. Fortunately, nonuniform FFTs (NUFFTs) provide a convenient trade-off in this sense [3–5, 8], being capable of reaching satisfactory accuracy with $\mathcal{O}(N \log N)$ complexity.

NUFFTs are not as uniquely defined as FFTs, having further degrees of algorithmic indeterminacy depending on the nonuniform domain and on the interpolating window used. Choosing the implementation that guarantees the most convenient trade-off between computational burden and accuracy is crucial.

Depending on whether the destination domain, the source domain, or both, are nonuniform, the NUFFT is respectively of nonequispaced-results (NER) type, nonequispaced-data (NED) type, or Type 3. NER and NED NUFFTs are of interest here.

The key of NUFFTs is the setup of the interpolating window. In [4, 5], we presented an optimized window design, based on a general and new perspective, for all three types of NUFFTs and extendable to any dimensions. The window was optimized to obtain more accurate results than those available in the literature without burdening computational and memory. The approach was presented for the 1-D case only.

The purpose here is to extend [4, 5] to 2-D for the NER and NED cases and apply the "optimized" 2-D NER and NED NUFFTs to spiral MRI under a 2-D geometry.

MRI reconstruction is tackled by filtered back-projection (FBP), which is of current interest [9–11] as a benchmark for other inversion schemes [12], as a starting guess for iterative approaches [13], or as the core of iterative methods [14]. FBP requires a single Fourier transform inversion and thus a NED NUFFT. However, alternative iterative approaches [15] involve, in addition to the inverse mapping, the direct one associated to a NER NUFFT. Therefore, we include discussions on the NER case as well. If an accurate algorithm is available without burdening the computation, there is no point in using a less accurate one. Using less accuracy is meaningful only if the complexity is reduced. Here we deal with the method leading to the best trade-off between complexity and accuracy. The performance is not evaluated in terms of computation time; the time performance of actual implementations depends on software/hardware factors, such as memory latencies or exploitation of cache memories and pipelines [16], which are beyond our scope. Nevertheless, proper implementations enable NUFFTs with operation counts consistent with $\mathcal{O}(N \log N)$ [17] and running in convenient times as compared to other, simpler interpolation schemes [12]. In MRI, qualitative or quantitative reconstructions are possible, with the latter case requiring high accuracy. In those systems, different sources of error can be present, including processing. The aim here is to show that the NUFFT error can be arbitrarily reduced up to machine precision without burdening the accuracy, and that from the perspective of more accurate MRI systems, the numerical accuracy will be by no means a limitation.

As the NUFFT aims to quickly compute a nonuniform discrete Fourier transform (NUDFT), we evaluate its accuracy as the closeness to the corresponding NUDFT [17].

2. MRI Model and FBP Inversion

In a 2-D geometry and for a generic interleaved trajectory, the signal r relates to the spin density ρ [1] as

$$r\left(k_x^\theta(t), k_y^\theta(t)\right) = \iint_O S(x,y)\rho(x,y)e^{-j2\pi\left[k_x^\theta(t)x + k_y^\theta(t)y\right]}dO \tag{1}$$

where S is the receiver-coil sensitivity map, $\underline{k}^\theta(t) =$

Manuscript received 21 August 2020.

Amedeo Capozzoli, Claudio Curcio, and Angelo Liseno are with Universitá di Napoli Federico II, DIETI, via Claudio 21, I 80125 Napoli, Italy; e-mail: a.capozzoli@unina.it.

$\left(k_x^\theta(t), k_y^\theta(t)\right)$ denotes the k-space trajectory, t is the time, θ is the interleave parameter, O is the investigated region, and $r\left(k_x^\theta(t), k_y^\theta(t)\right)$ is the Fourier transform of $S(x, y)\rho(x, y)$ evaluated at the spectral point $\left(k_x^\theta(t), k_y^\theta(t)\right)$. By changing θ and t, we acquire the value of r at different spectral points.

We deal with $S(x, y) = 1$ or, equivalently, with S absorbed in ρ, and with a square $O = [-a, a] \times [-a, a]$.

In FBP, the reconstruction $\rho_R(x, y)$ is expressed as the truncated inverse Fourier transform of (1) in polar coordinates [18].

We deal with $k_x^\theta(t)$ and $k_y^\theta(t)$ as the real and imaginary parts of a complex number k—i.e., $k^\theta(t) = k_x^\theta(t) + jk_y^\theta(t) = |k(t)|e^{j\underline{k(t)}+\theta}$, where the master spiral is rotated by θ to the generic interleave. Here, we set

$$k(t) = \mu\tau^\alpha(t)e^{j\omega\tau(t)} \tag{2}$$

where α, μ, and ω are parameters and the function $\tau(t)$ is set according to prescribed constraints (see [2]).

Let us ideally assume that by varying t and θ, the k-space trajectory $\left(k_x^\theta(t), k_y^\theta(t)\right)$ continuously fills a circular domain A_K centered around the origin and with radius K. Using polar coordinates (a, ϕ) in the spectral domain and with the change of variables [18] $a(t) = |k(t)| = \mu\tau^\alpha(t)$ and $\phi(t, \theta) = /\underline{k(t)} + \theta = \omega\tau(t) + \theta$ having Jacobian $J(t) = |dk/dt| \cdot |\cos(\underline{dk}/dt, k(t))|$, where $\cos(\cdot, \cdot)$ is the cosine of the phase difference between $k(t)$ and dk/dt, we can express the reconstruction as

$$\begin{aligned}\rho_R(x,y) = \int_0^{T_s}\int_0^{2\pi} & \mu\tau^\alpha(t)r(\mu\tau^\alpha(t)\cos(\omega\tau(t)+\theta), \\ & \mu\tau^\alpha(t)\sin(\omega\tau(t)+\theta)) \\ & e^{j2\pi\mu\tau^\alpha(t)[\cos(\omega\tau(t)+\theta)x+\sin(\omega\tau(t)+\theta)y]}J(t)dtd\theta\end{aligned} \tag{3}$$

which expresses the spiral FBP formula.

Using a pixel-based approximation of ρ with values computed on a regular Cartesian grid (x_h, y_l) and sampling r at the spectral locations given by uniformly spaced time instants t_n and uniformly spaced interleaves θ_k, (1) discretizes, for the generic interleave, as

$$r_{nk} = \sum_{hl}\rho_{hl}e^{-j2\pi\left[k_x^{\theta_k}(t_n)h\Delta x + k_y^{\theta_k}(t_n)l\Delta y\right]}\Delta x\Delta y, \quad n = 1, \ldots, N \tag{4}$$

where $r_{nk} = r\left(k_{x_n}^{\theta_k}, k_{y_n}^{\theta_k}\right)$, $k_{x_n}^{\theta_k} = k_x^{\theta_k}(t_n)$, $k_{y_n}^{\theta_k} = k_y^{\theta_k}(t_n)$, $\rho_{hl} = \rho(x_h, y_l)$ are the unknown pixel values, $(\Delta x, \Delta y)$ is the pixel size, and N is the overall number of samples. Of course, having assumed $a = b$, we know that $\Delta x = \Delta y$.

Finally, on assuming uniform temporal and angular discretizations Δt and $\Delta\theta = 2\pi/P$, (3) discretizes as

$$\rho_R(x_h, y_l) = \sum_{nk}\tilde{r}_{nk}e^{j2\pi\left[k_{x_n}^{\theta_k}x_h + k_{y_n}^{\theta_k}y_l\right]} \tag{5}$$

where $\tilde{r}_{nk} = \Delta\theta\Delta t\mu\tau^\alpha(t_n)J(t_n)r\left(k_{x_n}^{\theta_k}, k_{y_n}^{\theta_k}\right)$.

3. NUFFT-Based FBP and Optimized NUFFTs

The expression of the 2-D NED NUDFT of samples $\{z_s\}_{s=1}^S$ located at nonequispaced points $\{(\xi_s, \eta_s)\}_{s=1}^S$ belonging to $\left[-\frac{H}{2}, \frac{H}{2}\right] \times \left[-\frac{L}{2}, \frac{L}{2}\right]$ and evaluated at an equispaced grid is

$$\hat{z}_{hl} = \sum_{s=1}^{S} z_s e^{-j2\pi\xi_s\frac{h}{H}}e^{-j2\pi\eta_s\frac{l}{L}} \tag{6}$$

With the introduction of the index $s = s(n, k)$, (5) can be cast as a 2-D NED NUDFT. Accordingly, its computation can be accelerated by a 2-D NED NUFFT. Similarly, it can be seen that (4) can be accelerated by a 2-D NER NUFFT.

The optimized NUFFT properly interpolates the nonuniformly sampled exponentials $e^{-j2\pi\xi_s\frac{h}{H}}$ and $e^{-j2\pi\eta_s\frac{l}{L}}$ in (6) by uniformly sampled exponentials $e^{jm\lambda}$ [3–5] according to the Poisson summation formula [4, 5]:

$$e^{-jx\lambda} = \frac{(2\pi)^{-1/2}}{\hat{\phi}(\lambda)}\sum_{m\in Z}\hat{\phi}(x-m)e^{-jm\lambda}, |\lambda| \le \pi/c, \forall x \in \mathbb{R} \tag{7}$$

where $\phi(\lambda)$ is a window having compact support $(-\pi/c, \pi/c)$, c is an oversampling factor, and $\hat{\phi}(x)$ is its Fourier transform. The window ϕ is matter of choice. To be of interest, ϕ must be essentially bounded to $[-K, K]$ to ensure a finite summation in (7).

In our approach, for fixed values of K and c, ϕ is chosen as the window minimizing the representation error of $e^{-j\lambda x}$ in (7) when the summation on the right-hand side is truncated to a finite number of $2K + 1$ terms. Since ϕ must be compactly supported and $\hat{\phi}$ must be essentially compactly supported in $[-K, K]$, ϕ must belong to the space of the prolate spheroidal wave functions (PSWFs) corresponding to the singular values of the Fourier transform operator before the knee [4, 5]. In other words,

$$\phi(\lambda) = \sum_{t=0}^{T}\gamma_t\Psi_{2t}[w, \lambda] \tag{8}$$

where Ψ_k denotes the kth PSWFs with space-bandwidth product w, T the number of expansion functions, and γ_t the unknown expansion coefficients. Owing to the symmetry of ϕ, in (8) only the PSWFs with even order (even symmetry) are considered. To enforce the desired properties, the space-bandwidth product is chosen as

$$w = \chi\left(2\pi - \frac{\pi}{c}\right)K \tag{9}$$

where χ is a coefficient which can be subject to further

Table 1. Accuracy of 2D NER NUFFT

c	K	χ_{opt}	RMS KB	RMS opt	RMS Fessler	Max KB	Max opt	Max Fessler
1.5	3	1.5	5.88×10^{-3}	1.34×10^{-3}	6.61×10^{-3}	8.03×10^{-4}	1.68×10^{-4}	1.26×10^{-1}
2	3	1.2	4.99×10^{-4}	8.45×10^{-5}	4.99×10^{-4}	5.90×10^{-5}	1.08×10^{-5}	1.63×10^{-3}
1.5	6	1.1	8.65×10^{-8}	2.28×10^{-8}	8.65×10^{-8}	9.85×10^{-9}	3.16×10^{-9}	5.37×10^{-3}
2	6	1.2	7.31×10^{-10}	1.77×10^{-10}	N/A	7.68×10^{-11}	1.56×10^{-11}	N/A

optimization. The number of retained expansion PSWFs is chosen as $2T \leq \lfloor (2w/\pi) \rfloor$, where $\lfloor v \rfloor$ is the largest integer smaller than v. In this way, ϕ has compact support in $[-\chi(2\pi - (\pi/c)), \chi(2\pi - (\pi/c))]$ and $\hat{\phi}$ is essentially supported in $[-K, K]$.

The expansion coefficients $\underline{\gamma}$ of the PSWFs are determined [4, 5] to optimize the functional

$$\Gamma(\underline{\gamma}) = \int_{-x_M}^{x_M} \int_{-\pi/c}^{\pi/c} d\lambda dx \left| e^{-jx\lambda} - \frac{(2\pi)^{-1/2}}{\phi(\lambda; \underline{\gamma})} \sum_{|m| \leq K} \hat{\phi}\left(x - (\lfloor x \rfloor + m); \underline{\gamma}\right) e^{-j(\lfloor x \rfloor + m)\lambda} \right|. \tag{10}$$

Provided a sufficiently large x_M is used in the numerical minimization, the optimization of $\Gamma(\underline{\gamma})$ depends only on c and K, not on the number or locations of the input/output points. The parameters c and K should be chosen according to the required accuracy. For example, $c = 1.5$ and $K = 3$ corresponds to single precision, $c = 2$ and $K = 6$ to double precision. Changing c and K changes the result of the optimization of (10)—i.e., the optimal expansion coefficients $\underline{\gamma}$—but the procedure is automatic. Given the expansion coefficients, the window ϕ is uniquely defined. Since, as already mentioned, ϕ depends at the end only on c and K, the optimal coefficients $\underline{\gamma}$ can be stored and recycled, as there is no need to repeat the optimization for different MRI setups. Some expansion coefficients of ϕ in terms of Legendre polynomials for different choices of c and K can be found in [19].

A detailed description of the NED NUFFT is reported in [20]; the NER NUFFT follows similar guidelines.

4. Numerical and Experimental Results

We now first assess the accuracy of the optimized 2-D NUFFTs for different computational loads in comparison with other approaches from the literature, namely, the Kaiser–Bessel (KB) scheme [3] and Fessler's scheme [1]. As mentioned in the Introduction, the accuracy is assessed by comparing the NUFFT output and the corresponding NUDFT one.

For the NER case, 100 random sequences have been transformed, with $(H, L) = (12, 12)$ and uniformly distributed real and imaginary parts, both in $[-1/2, 1/2]$. A number $N = 12 \times 12$ of random output sampling points has been considered, uniformly distributed in $(-H/4, H/4) \times (-L/4, L/4)$. Table 1 reports the worst-case results of the comparison in terms of percentage root-mean-square and maximum errors. Fessler's scheme is unavailable for the case where $c = 2$ and $K = 6$.

Our optimized NUFFT outperforms Fessler's approach by different orders of magnitude, while it gains up to almost one order of magnitude with respect to the KB case. Also, by controlling c and K it is possible to progressively increase the accuracy of the NUFFT, which can ultimately be driven very close to machine precision.

In the NED case, random elements have been considered, again with uniformly distributed real and imaginary parts in $[-1/2, 1/2]$. The output has been evaluated on a uniform grid with $(H, L) = (72, 72)$. Table 2 reports the results of the comparisons, and the same observations apply as for the NER case.

The performance and the convenience of the optimized NUFFT on spiral-trajectory MRI simulated data are now assessed.

In particular, a test case with a 0.2 m $\times$ 0.2 m region of interest discretized by 1024×1024 pixels has been considered. A spiral acquisition has been dealt with that has 30 interleaves and $\lambda = 0.55/\Delta x$. The test case comprises the Shepp–Logan phantom, a typical numerical reference to benchmark imaging algorithms.

Figure 1 shows the reference phantom, while Figure 2 illustrates the reconstruction, which confirms the predicted accuracy. Figure 3 highlights the cuts along the x-axis of the reconstruction errors for the three compared algorithms.

We finally show results obtained on experimental data. The data were acquired on a 3T MRI scanner with a 220 mm $\times$ 292 mm field of view and using 18 interleaved spirals [21]. The experimental reconstruction is illustrated in Figure 4.

Table 2. Accuracy of 2D NED NUFFT

c	K	χ_{opt}	RMS KB	RMS opt	RMS Fessler	Max KB	Max opt	Max Fessler
1.5	3	1.5	3.14×10^{-3}	6.54×10^{-4}	3.36×10^{-3}	5.68×10^{-3}	1.16×10^{-3}	2.18
2	3	1.2	3.99×10^{-4}	6.17×10^{-5}	1.38×10^{-2}	6.04×10^{-4}	1.09×10^{-4}	1.21×10^{-2}
1.5	6	1.1	5.06×10^{-8}	9.21×10^{-9}	3.34×10^{-2}	7.63×10^{-8}	2.04×10^{-8}	3.06×10^{-2}
2	6	1.2	5.41×10^{-10}	8.57×10^{-11}	N/A	6.83×10^{-10}	1.44×10^{-10}	N/A

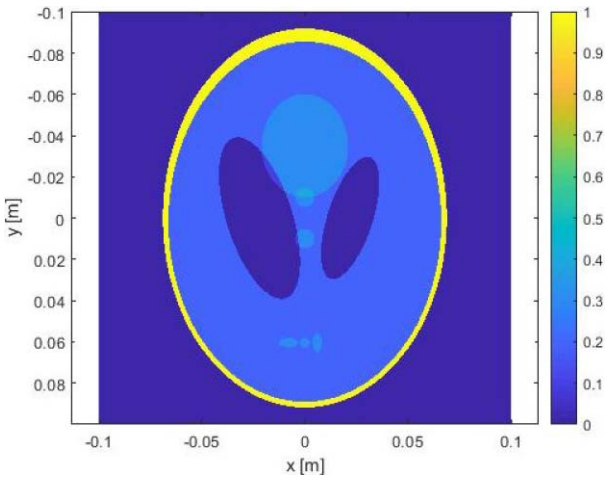

Figure 1. The Shepp–Logan phantom.

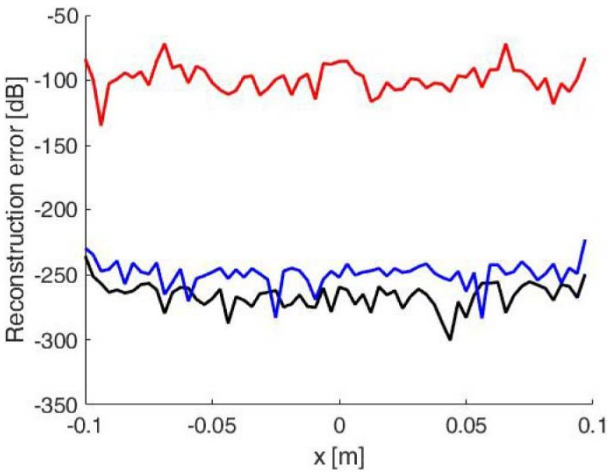

Figure 3. The x-cut of the reconstruction error. Red: Fessler; blue: KB; black: optimized.

5. Conclusions and Future Developments

We have dealt with MRI spiral sampling trajectory. The approach in [4, 5] has been extended to 2-D and its accuracy assessed against approaches from the literature. Our approach is capable of modulating computational complexity and accuracy by a proper choice of c and K, thus reducing the accuracy in favor of processing speed, if necessary. Modulating accuracy and complexity is possible until almost-exact transforms are reached. The achieved maximum error of 10^{-11} means accuracy approaching the best possible in double precision. In such circumstances, the source of any inaccuracy should be sought in places other than the NUFFTs. Also, the approach gains up to almost one order of magnitude in accuracy against the KB scheme, and several orders of magnitude against the method in [1].

First results on using NUFFTs in MRI with radial trajectories have been obtained reaching similar accuracy. The NUFFTs are also of interest when gradient-based, iterative schemes are used. In this context, highly accurate NER and NED NUFFTs help prevent error accumulation which could impair their convergence [22]. NUFFT-based FBP is even of interest in other domains of tomography, as computed tomography [9], nuclear medicine [9], and microwave imaging [23]. For highly undersampled, non-Cartesian acquisitions, when information such as piecewice constancy can be exploited, regularization techniques such as total variation can be exploited. In such algorithms, the inversion is iterative and the iterated application of forward and inverse numerical operators can lead to error accumulation. In particular, the incorporation of a NUFFT-based FBP appears quite advantageous since, thanks to its accuracy, it is capable of controlling the number of iterations [24]. Type 3 NUFFTs [8] can be of interest when a non-uniform spatial resolution is desired.

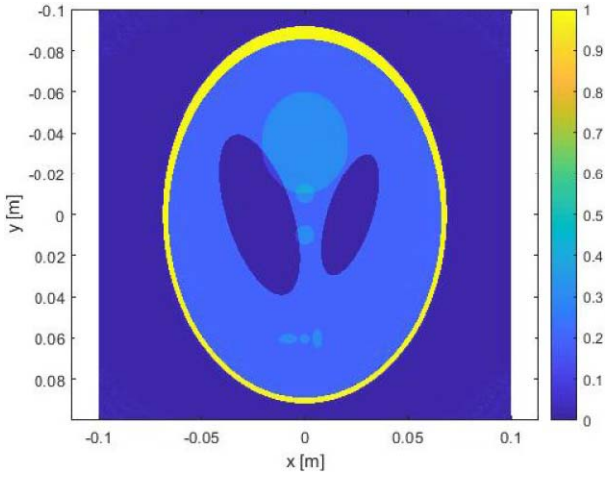

Figure 2. Spiral reconstruction.

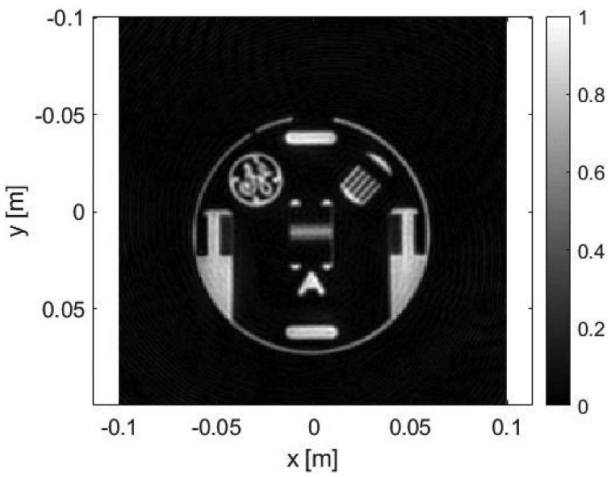

Figure 4. Experimental reconstruction.

6. References

1. J. A. Fessler, "On NUFFT-Based Gridding for Non-Cartesian MRI," *Journal of Magnetic Resonance*, **188**, 2, October 2007, pp. 191-195.
2. D.-H. Kim, E. Adalsteinsson, and D. M. Spielman, "Simple Analytic Variable Density Spiral Design," *Magnetic Resonance in Medicine*, **50**, 1, July 2003, pp. 214-219.
3. K. Fourmont, "Non-Equispaced Fast Fourier Transforms With Applications to Tomography," *Journal of Fourier Analysis and Applications*, **9**, 5, September 2003, pp. 431-450.
4. A. Capozzoli, C. Curcio, and A. Liseno, "An Approach to NUFFT Optimization," XXII Riunione Nazionale di Elettromagnetismo, Caligari, Italy, September 3–6, 2018, pp. 9-10.
5. A. Capozzoli, C. Curcio, and A. Liseno, "Optimized Nonuniform FFTs and Their Application to Array Factor Computation," *IEEE Transactions on Antennas and Propagation*, **67**, 6, June 2019, pp. 3924-3938.
6. C. K. Turnes and J. Romberg, "Efficient Calculations of 3-D FFTs on Spiral Contours," *Journal of Scientific Computing*, **50**, 3, March 2012, pp. 610-628.
7. A. G. Sorace, C. Wu, S. L. Barnes, A. M. Jarrett, S. Avery, et al., "Repeatability, Reproducibility, and Accuracy of Quantitative MRI of the Breast in the Community Radiology Setting," *Journal of Magnetic Resonance Imaging*, **48**, 3, September 2018, pp. 695-707.
8. A. Capozzoli, C. Curcio, A. Liseno, and A. Riccardi, "Parameter Selection and Accuracy in Type-3 Non-Uniform FFTs Based on Gaussian Gridding," *Progress in Electromagnetics Research*, **142**, 2013, pp. 743-770.
9. G. L. Zeng, "Model Based Filtered Backprojection Algorithm: A Tutorial," *Biomedical Engineering Letters*, **4**, 1, March 2014, pp. 3-18.
10. Y. Yang, F. Liu, M. Li, J. Jin, E. Weber, et al., "Pseudo-Polar Fourier Transform-Based Compressed Sensing MRI," *IEEE Transactions on Biomedical Engineering*, **64**, 4, April 2017, pp. 816-825.
11. G. L. Zeng and E. V. DiBella, "Non-Iterative Image Reconstruction From Sparse Magnetic Resonance Imaging Radial Data Without Priors," *Visual Computing for Industry, Biomedicine, and Art*, **3**, April 2020, p. 9.
12. J. Park, J. Lee, J. Lee, S.-K. Lee, and J.-Y. Park, "Strategies for Rapid Reconstruction in 3D MRI With Radial Data Acquisition: 3D Fast Fourier Transform vs Two-Step 2D Filtered Back-Projection," *Scientific Reports*, **10**, 1, August 2020, p. 13813.
13. J. Adler and O. Öktem, "Learned Primal-Dual Reconstruction," *IEEE Transactions on Medical Imaging*, **37**, 6, June 2018, pp. 1322-1332.
14. G. L. Zeng and Z. Divkovic, "An Extended Bayesian-FBP Algorithm," *IEEE Transactions on Nuclear Medicine*, **63**, 1, February 2016, pp. 151-156.
15. Y. Lei, J. Harms, T. Wang, S. Tian, J. Zhou, et al., "MRI-Based Synthetic CT Generation Using Semantic Random Forest With Iterative Refinement," *Physics in Medicine and Biology*, **64**, 8, April 2019, p. 085001.
16. M. Frigo and S. G. Johnson, "The Design and Implementation of FFTW3," *Proceedings of the IEEE*, **93**, 2, February 2005, pp. 216-231.
17. A. Capozzoli, C. Curcio, G. D'Elia, A. Liseno, and P. Vinetti, "Fast CPU/GPU Pattern Evaluation of Irregular Arrays," *Applied Computational Electromagnetics Society Journal*, **25**, 4, April 2010, pp. 355-372.
18. R. D. Hoge, R. K. S. Kwan, and G. B. Pike, "Density Compensation Functions for Spiral MRI," *Magnetic Resonance in Medicine*, **38**, 1, July 1997, pp. 117-128.
19. "Legendre Coefficients Representing The Optimized Window," https://archive.org/details/LegendreCoefficientsRepresentingTheOptimizedWindow (Accessed December 03, 2020).
20. A. Capozzoli, C. Curcio, A. Liseno, and G. Toso, "Fast, Phase-Only Synthesis of Aperiodic Reflectarrays Using NUFFTs and CUDA," *Progress in Electromagnetics Research*, **156**, June 2016, pp. 83-103.
21. Haldar, J. P. (NSF grant CCF-1350563), "Real MRI Dataset Samples," ' https://mr.usc.edu/download/data/ (Accessed December 03, 2020).
22. H. Kajbaf, J. T. Case, Z. Yang, and Y. R. Zheng, "Compressed Sensing for SAR-Based Wideband Three-Dimensional Microwave Imaging System Using Non-Uniform Fast Fourier Transform," *IET Radar, Sonar & Navigation*, **7**, 6, July 2013, pp. 658-670.
23. A. Capozzoli. C. Curcio, A. di Vico, and A. Liseno, "NUFFT- & GPU-Based Fast Imaging of Vegetation," *IEICE Transactions on Communications*, **E94-B**, 7, July 2011, pp. 2092-2103.
24. X. Duan, L. Zhang, Y. Xing, Z. Chen, and J. Cheng, "Few-View Projection Reconstruction With an Iterative Reconstruction-Reprojection Algorithm and TV Constraint," *IEEE Transactions on Nuclear Science*, **56**, 3, June 2009, pp. 1377-1382.